Liquid Invasion from Multiple Inlet Sources and Optimal Gas Access in a Two-Layer Thin Porous Medium

N. Belgacem[1,3] · **T. Agaësse**[1,3] · **J. Pauchet**[3] · **M. Prat**[1,2]

Abstract This study builds upon previous work on single-layer invasion percolation in thin layers to incorporate a second layer with significantly different pore sizes and to study the impact of the resulting water configuration on gas-phase mass transport. We consider a situation where liquid water is injected at the assembly inlet through a series of independent injection points. The challenge is to ensure the transport of the liquid water while maintaining a good diffusive transport within the gas phase. The beneficial impact of the fine layer on the gas diffusion transport is shown. It is further shown that there exists a narrow range of fine layer thicknesses optimizing the gas transport. The results are discussed in relation with the water management issue in polymer electrolyte membrane fuel cells. Additional discussions, of more general interest in the context of thin porous system, are also offered.

Keywords Thin porous media · Invasion percolation · Pore network simulation · Polymer electrolyte fuel cell

1 Introduction

As discussed in Prat and Agaësse (2015), the modeling of transport phenomena in thin porous media (TPM) poses specific questions. This is notably so because the traditional modeling tools, such as the classical volume-averaged transport equations, cannot often be used at all or cannot be used in their traditional forms (e.g., Qin and Hassanizadeh 2014). This is especially true for the TPM with only a few pores over their thickness because the traditional concept of

✉ M. Prat
mprat@imft.fr

1 INPT, UPS, IMFT (Institut de Mécanique des Fluides de Toulouse), Université de Toulouse, Allée Camille Soula, 31400 Toulouse, France

2 CNRS, IMFT, 31400 Toulouse, France

3 Fuel Cell Components Laboratory (LCPEM), LITEN CEA, 17 rue des Martyrs, 38000 Grenoble, France

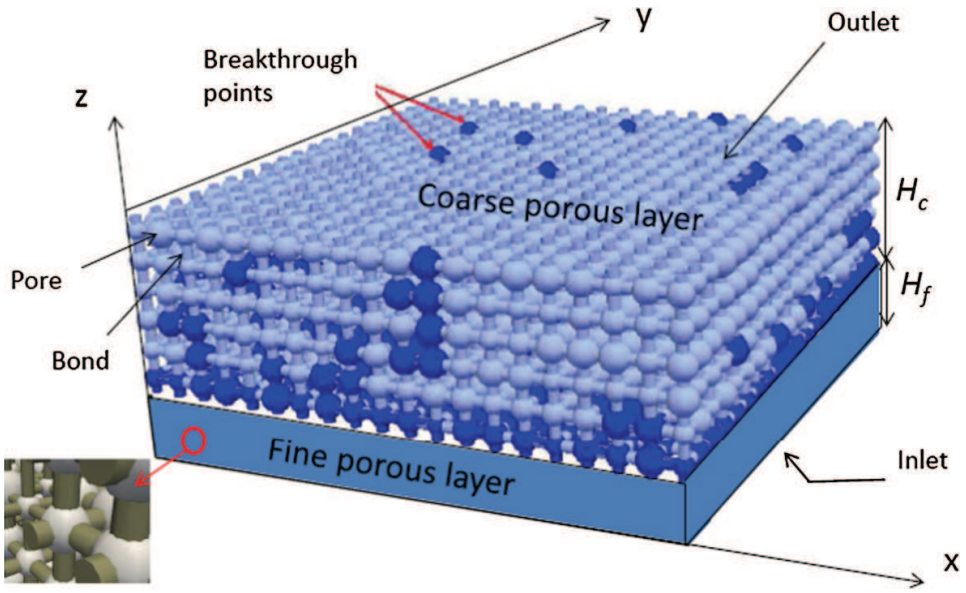

Fig. 1 Sketch of the problem considered in this study. Liquid water (in *blue*) is injected at the inlet of the fine layer through a series of independent injection bonds and percolates through the assembly up to the outlet where it forms droplets (referred to as breakthrough points). A gaseous species is transported by diffusion between the outlet surface and inlet surface in the gas phase (pores and bonds shown in *light blue gray* in the coarse layer; the various phases are not illustrated in the fine layer)

length scale separation underlying the classical Darcy scale equations is not satisfied over the thickness. In the present article, we consider a quite different approach, not based on volume-averaged or thickness-averaged equations or any other types of up-scaled partial differential equations (PDE). Instead, transfer "laws" are established from a series of extensive pore network simulations and it is shown how these laws can be used to predict the properties of the considered thin system. The idea is not to determine local fields but rather to determine the response of the entire thin system. Thus, from a methodological standpoint, the objective is to enrich the TPM tool box with the consideration of an approach not based on up-scaled PDE.

The approach is presented from the consideration of the problem depicted in Fig. 1. A thin hydrophobic porous medium is formed by the assembly of two porous layers. The lateral extension of this system is typically on the order of 2–3 mm. A coarser porous layer is on top. The thickness of this layer is typically on the order of 200–300 μm with an average pore size of 30–50 μm. A thinner porous layer, hereafter called the fine layer, forms the bottom layer. The average pore size in this layer is on the order of 500 nm, thus about ten times smaller than in the coarse layer. The system inlet is formed by the bottom surface of the fine layer, whereas the outlet is formed by the coarse layer top surface (Fig. 1). Initially, all the pores are occupied by the gaseous phase. The latter is a mixture of several species, and we will be interested in the diffusive transport of one of these species across the two-layer assembly between the outlet and the inlet (gas transport is on average in the direction opposite to that of liquid flow). Liquid water is then injected at the inlet, thus at the entrance of the fine layer until it reaches the outlet on top of the coarse layer. This corresponds to the liquid breakthrough. It is assumed that all the water reaching the outlet is immediately removed owing to the gas flow existing along the outlet surface. This means that there is no influence of transfers at the outlet surface on the gas–liquid distribution within the porous system.

At the inlet liquid water is injected through a series of independent injection points. Let denote the number of injection points by N_i. N_i can vary between 1 and $N_{i\,\max}$ where $N_{i\,\max}$ is the number of entry pores at the fine layer inlet.

The objective is then to predict the number of breakthrough points at the system outlet and the liquid saturation in both the fine layer and the coarse layer and to characterize the gas access to the inlet. As discussed in Ceballos and Prat (2010), breakthrough points correspond to droplet formation spots at the outlet surface. Those droplets represent observable data. Determining their number is therefore interesting to characterize the two-phase flow in the system under study.

This problem was studied in previous publications (i.e., Ceballos and Prat 2010; Ceballos et al. 2011; Ceballos and Prat 2013). However, the system was formed only by the coarse layer without the fine layer. The impact of the fine layer was thus not studied. Hence, this study builds upon previous work on single-layer invasion percolation in thin layers to incorporate (i) a second layer with significantly different pore sizes but otherwise similar behavior and (ii) the impact of the resulting water configuration on gas-phase mass transport. Also, we provide in the present article simple theoretical arguments supporting the detailed numerical results reported in Ceballos (2011). Additional pore network simulations on random networks are also presented to confirm the universal nature of the results used in the present work.

This problem is inspired from a situation encountered in a polymer electrolyte membrane fuel cell (PEMFC) (e.g., Barbir 2005). However, there is no need to be familiar with PEMFC to understand the present article. The PEMFC terminology is not used in what follows except in a subsection in Sect. 6 where the results are briefly discussed in relation with PEMFC. This subsection can be skipped by readers not interested in PEMFC.

The paper is organized as follows. The main results presented in previous papers and useful for the present paper are briefly recalled in Sect. 2. New results for a single coarse layer are presented in Sect. 3 together with the theoretical arguments. The properties of fine layer are given in Sect. 4. The main part of the paper, i.e., the study of the fine layer–coarse layer assembly, is presented in Sect. 5. Discussions are presented in Sect. 6. These notably include a brief discussion of main results in relation with the water management issue in PEMFC and a discussion about the modeling of the fine layer–coarse layer interface. Conclusions are presented in Sect. 7.

2 Literature Review

Capillarity-controlled two-phase flows in thin layers have motivated many studies in recent years in relation with the problem of the water management in PEMFC, a crucial aspect of this technology. As for the present work, many of these studies are based on pore network models (PNM) (e.g., Sinha and Wang 2007; Markicevic et al. 2007; Bazylak et al. 2008; Hinebaugh et al. 2010; Lee et al. 2009, 2010, 2014; Gostick 2013; Wu et al. 2013; Fazeli et al. 2015; Quin 2015).

The majority of these studies used the traditional invasion percolation algorithm (e.g., Wilkinson and Willemsen 1983; Sheppard et al. 1999). However, as discussed in Ceballos and Prat (2010), the boundary condition of uniform pressure at the inlet used in classical IP simulations can be questioned in the context of PEMFC studies. In particular, the classical boundary condition is not consistent with the in situ observations showing several breakthrough points at the outlet of the thin layer since only one breakthrough point is obtained using the traditional version of the IP algorithm. This led to the consideration of a different inlet boundary condition where the non-wetting fluid is injected through a series of independent injection points at the inlet. As shown in Ceballos and Prat (2010), the surface density of breakthrough points is then consistent with the observations. The impact of this boundary

condition was then studied in detail in Ceballos et al. (2011) and Ceballos and Prat (2013). We are not aware of previous works in the context of IP theory where the IP variants considered in Ceballos and Prat (2010) and Ceballos et al. (2011) were studied.

In this section, we recall some of the results presented in Ceballos et al. (2011) and Ceballos and Prat (2013) which are useful for the present study. These results were obtained using a simple cubic pore network. In this model, the pores are located at the nodes of a cubic mesh. Two adjacent pores are connected by a narrower channel called bond. The pore and bond sizes are randomly distributed according to given probability density functions. The size of the cubic network was denoted by $L \times L \times H$, where H was the porous medium thickness or $N_x \times N_y \times N_z$ (with $N_x = N_y$) measured in number of pores along each direction of a Cartesian coordinate system. In this pore network model, the inlet is formed by N_x^2 bonds oriented in the z direction giving access to the N_x^2 pores located in the first x–y plane of pores. Liquid is injected through these bonds, which are thus referred to as "injection points" or "injection bonds." The number of injection points was defined via the fraction n_i of injection points at the inlet, $n_i = N_i/N_x^2$, where N_i is the number of injection points. Thus, $n_i = 1$, for example, corresponds *to* $N_i = N_{i\,\max} = N_x^2$. The injection bonds were randomly selected at the inlet when $n_i < 1$. The impact of n_i was explored varying n_i in the range [0.02, 1]. Thus, fractions of inlet injection bonds lower than 2 % were not considered.

The pore network was hydrophobic, and the liquid water injection was supposed to be sufficiently slow for viscous effects to be negligible compared to capillary effects. Gravity effects are also negligible so that water invasion was simulated using a variant of the invasion percolation (IP) algorithm (Wilkinson and Willemsen 1983). As mentioned above, the variant lies in the boundary condition (multiple independent injection points versus a reservoir-type condition with the classical IP algorithm). Also, the coalescence between liquid paths originating from different liquid injection points is taken into account.

2.1 Liquid Invasion Simulation Algorithm

We used the simultaneous IP algorithm referred to as the sequential algorithm in Ceballos et al. (2011). The algorithm can be summarized as follows:

1. The network is fully saturated by the gas phase initially.
2. A first liquid flow path is computed using the standard IP algorithm without trapping starting from a first injection point (selected at random among the inlet active bonds or sequentially). The computation of this step stops at breakthrough, that is when the liquid water reaches the outlet.
3. The simulation is repeated starting from a second injection bond at the inlet. This second invasion stops either when the flow path generated from this second injection point merges into the flow path associated with the first injection bond (flow path coalescence) or at breakthrough, i.e., when the liquid injected from the second inlet bond reaches the outlet through a path independent from the path connected to the first injection point.
4. The procedure is repeated starting successively from all the other injection bonds at the inlet.

Simulations were performed with this algorithm over many realizations of the cubic network varying the thickness of the layer. The results were ensemble-averaged over the number of considered realizations. The results of interest for the present work are presented in Figs. 2, 3 and 4. These results were obtained for $N_x = N_y = 20$ and $N_x = N_y = 40$, varying N_z using random distributions of bond and pore sizes.

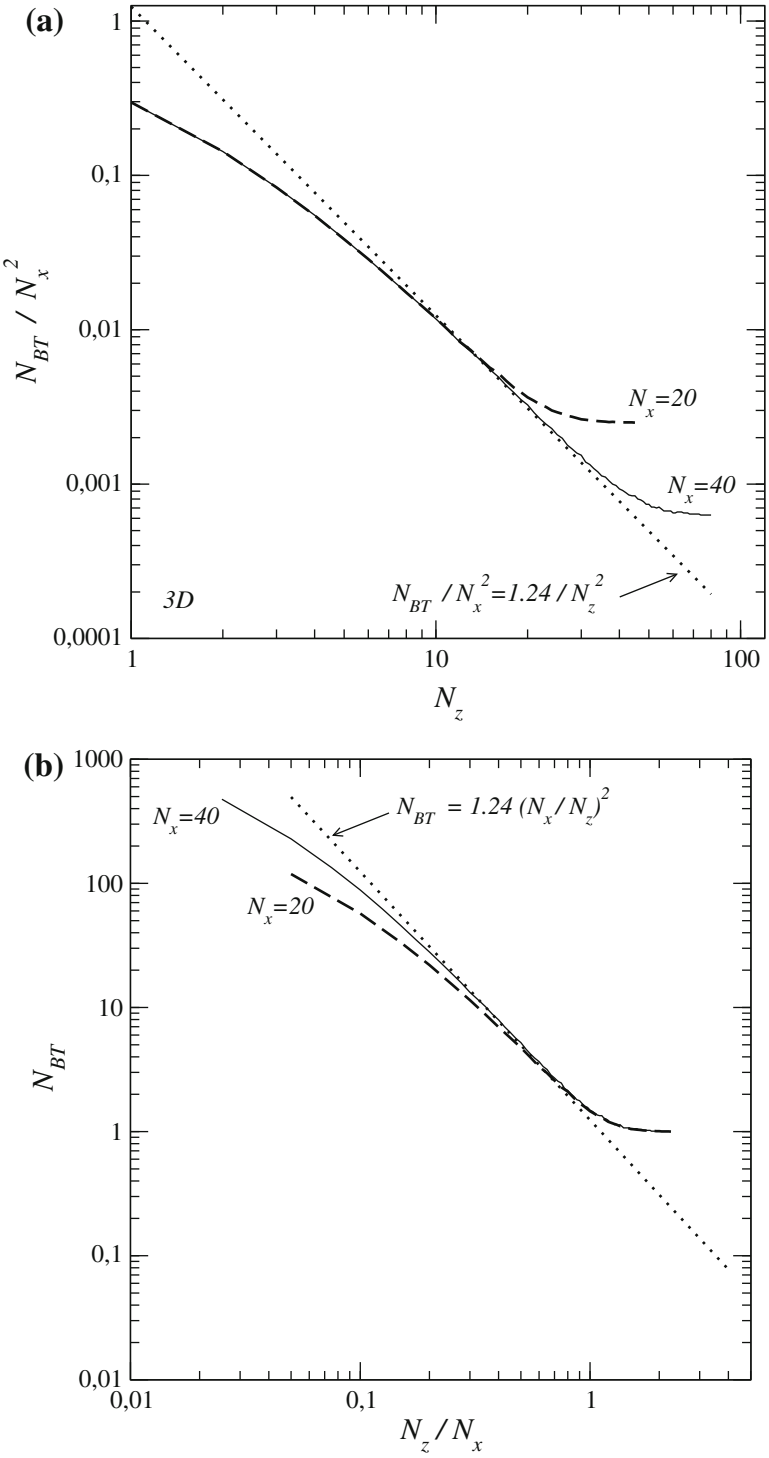

Fig. 2 **a** Probability that an outlet bond is a breakthrough point as a function of network thickness N_z when all inlet bonds are active at the inlet ($n_i = 100\,\%$). **b** Average number of breakthrough points N_{BT} as a function of porous layer relative thickness N_z/N_x when all pores are active at the inlet ($N_i = N_{\max}$) ($n_i = 100\,\%$). The results are shown for two network lateral sizes ($N_x = N_y = 20$ and $N_x = N_y = 40$)

2.2 Breakthrough Points

Figure 2a shows the probability that an outlet bond is a breakthrough point as a function of network thickness N_z, whereas Fig. 2b shows the average number of breakthrough points N_{BT} as a function of porous layer relative thickness N_z/N_x when all pores are active at the inlet ($n_i = 1$).

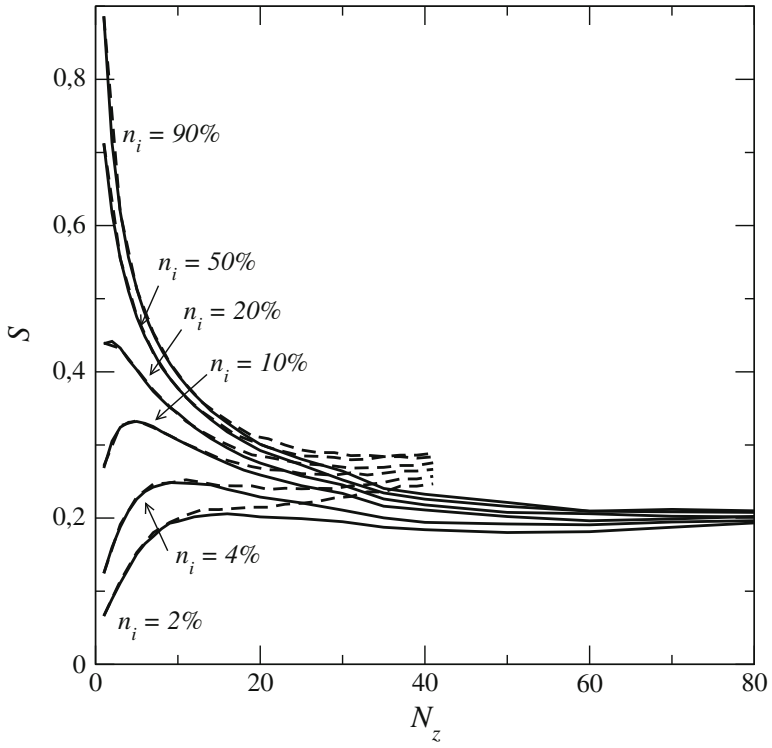

Fig. 3 Mean overall liquid saturation as a function of porous layer thickness for various injection point fraction n_i for two network lateral sizes [$N_x = N_y = 20$ (*dashed lines*) and $N_x = N_y = 40$ (*solid lines*)]

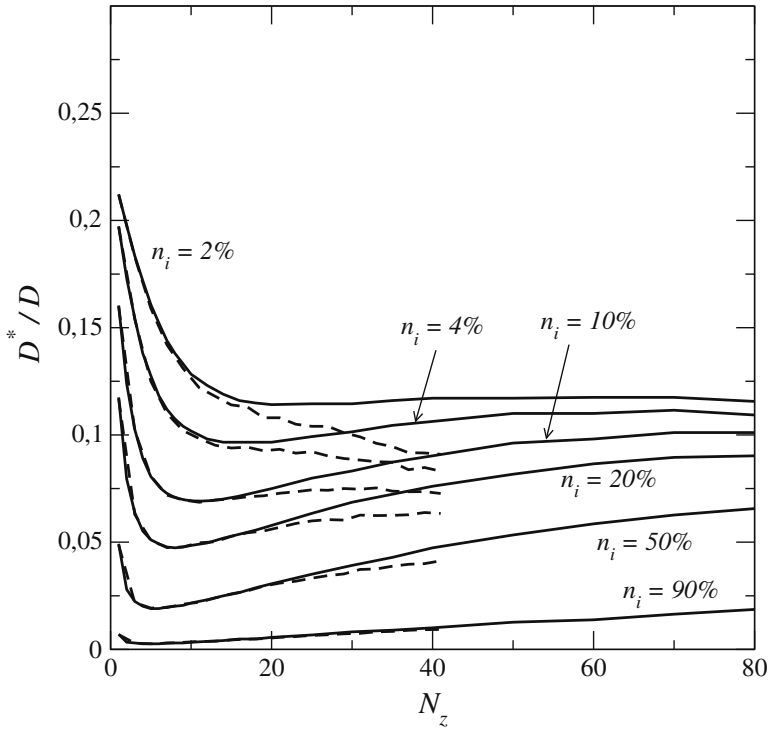

Fig. 4 Variation of effective diffusion coefficient as a function of network thickness for various injection point fraction n_i for two network lateral sizes [$N_x = N_y = 20$ (*dashed lines*) and $N_x = N_y = 40$ (*solid lines*)]

Four regions can be distinguished in Fig. 2a depending on the thickness N_z of the system: (1) the ultrathin system region when the system is sufficiently thin, i.e., $N_z \leq 10$, (2) the power law region for larger thicknesses right after the region of ultrathin systems where $N_{\mathrm{BT}}/N_x^2 \propto N_z^{-2}$, (3) a transition region between the power law region and region #4, (4) the

thick systems characterized by only one breakthrough point (plateaus on the right-hand side in Fig. 2a, noticing that only the beginning of plateaus is shown).

As can be seen from Fig. 2a, the behaviors of ultrathin and thin systems (power law region) is independent of lateral size, which means that N_{BT}/N_x^2 only depends on N_z in the ultrathin and thin porous medium domain. It is of course interesting to determine the range of validity of the universal behaviors corresponding to the ultrathin and the thin systems. As can be seen from Fig. 2b, the power law regime characterizing the thin systems is observed up to $N_z/N_x \approx 0.8$. Thus, for a given lateral size N_x, the universal behaviors are obtained as long as $N_z \leq 0.8N_x$. Universal behaviors mean here independent of lateral size. This can be expressed as

$$N_{BT}/N_x^2 = f(N_z, n_i) \quad \text{if} \quad N_z \leq 0.8\, N_x \tag{1}$$

where f is a function depending only on N_z for a given n_i.

Additional information not considered in the previous works is the distribution of breakthrough points at the outlet. There is no reason to expect something different from a homogeneous distribution [as long as N_{BT} is not too small, i.e., in the regime corresponding to Eq. (1)]. Assuming that the breakthrough points are evenly distributed at the surface, the mean distance d between two neighbor breakthrough points is then given by

$$\frac{d}{a} = \frac{2}{\sqrt{\pi f(N_z, n_i)}} \tag{2}$$

where a is the lattice spacing (distance between two neighbor pores in the network).

2.3 Overall Liquid Saturation

Somewhat similarly as for the breakthrough point statistics, the results reported in (Ceballos et al. 2011) show that the overall liquid saturation at the end of displacement only depends on N_z for a given fraction n_i of injection bonds at the inlet as long as $N_z < 20$. Thus,

$$S = f_s(N_z, n_i) \quad \text{if} \quad N_z < 20 \tag{3}$$

This is illustrated in Fig. 3.

3 Coarse Single-Layer Additional Results

3.1 Diffusion Coefficient

The gas phase is a binary mixture of two species A and B. The gas access is characterized by the diffusive flux of species B through the layer for a given concentration difference Δc imposed across the layer. This flux, denoted by J, can be expressed as

$$J \approx \frac{D^*}{H}\Delta c \tag{4}$$

where D^* is the effective diffusion coefficient of the layer; D^* can be computed from pore network simulations. We used the method described in Gostick et al. (2007).

Variations of D^* as a function of layer thickness computed from pore network simulations are shown in Fig. 4. Again an "universal" behavior is observed for the sufficiently thin systems,

$$\frac{D^*}{D} = f_D(N_z, n_i) \quad \text{if} \quad N_z \leq 20. \tag{5}$$

where D is the molecular diffusion coefficient of the considered species.

Note also the non-monotonous variation of D^* as a function of N_z. This non-monotonous variation may appear as counterintuitive since the variation of saturation in Fig. 3 is monotonously decreasing. In fact, the expected result is that the diffusive flux J decreases with N_z and this is indeed what is obtained (as shown in Fig. 6a in Ceballos and Prat (2013)). From Eq. (4), $D*$ can thus be interpreted as the product of an increasing function of $N_z (H = aN_z$, where a is the distance between two pores in the network) and a decreasing function of $N_z (= J)$. This can be expressed mathematically as $\frac{\partial D^*}{\partial H} \propto H \frac{\partial J}{\partial H} + J$ where $\frac{\partial J}{\partial H} < 0$ and $J > 0$. In the range of very low thicknesses, the variation of $D*$ is dominated by the term $H \frac{\partial J}{\partial H}$, and thus $\frac{\partial D^*}{\partial H} < 0$ whereas the variation for greater N_z is dominated by the term J, leading to $\frac{\partial D^*}{\partial H} > 0$.

3.2 Simple Theoretical Considerations

The universal behavior regarding the number of breakthrough points described in Sect. 2.2 can be predicted from a simple argument. We consider the situations where $N_z < N_x$. Figure 5 shows a pore network numerical simulation of the considered invasion scenario for $n_i = 1$. A colored cluster in the figure corresponds to the liquid cluster associated with one breakthrough point. Thus, there are 6 breakthrough points in this example. This figure clearly suggests that the system can be decomposed into a finite number of independent regions (the lateral limiting surfaces of a region act as capillary barriers for the liquid present in the adjacent regions). The liquid phase in each region is connected to only one breakthrough point.

Here we make the simplifying assumption that the size of an elementary region is approximately equal to its thickness. Thus, we decompose the system into a number of elementary cubes of lateral size N_z. There are N_b elementary cubes with $N_b = (N_x/N_z)^2$.

Suppose now that the number of breakthrough points is the same (in an average sense) for each cube independently of thickness N_z. This number is denoted by N_e. We do not take $N_e = 1$ a priori because we do not know whether the size of each elementary cube corresponds to the size of the clusters illustrated in Fig. 5, noting that the image in Fig. 5 is

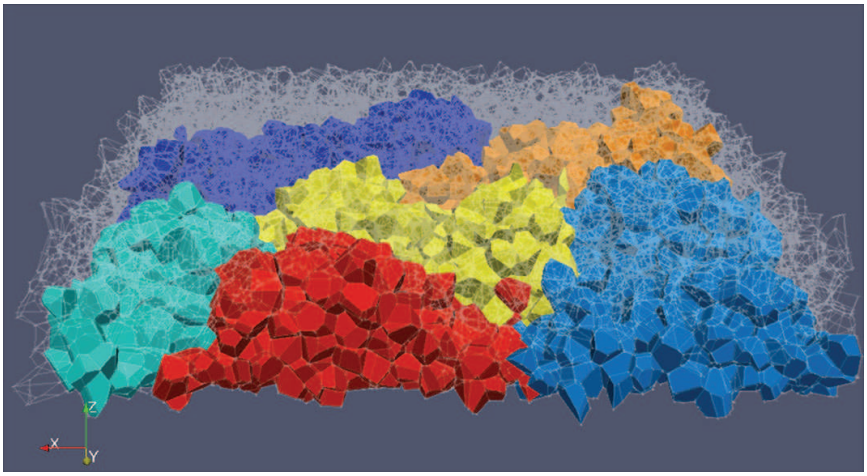

Fig. 5 Multiple injection scenario leads to the formation of a series of independent liquid occupied regions in the network. Each region is shown with a *different color* and is connected to only one breakthrough point. Hence, each breakthrough point is associated with a well-defined and individualized region of the system

for a small network and is merely illustrative. Then, the total number of breakthrough points is simply given by,

$$N_{\mathrm{BT}} \approx N_e (N_x/N_z)^2 \tag{6}$$

leading to

$$\frac{N_{\mathrm{BT}}}{N_x^2} \approx \frac{N_e}{N_z^2} \tag{7}$$

which perfectly corresponds to the power law regime depicted in Fig. 2a.

The numerical results on a cubic network indicate that $N_e \approx 1.24$. In fact, the numerical results for a network of size $N_x \times N_x \times N_x$ show that the number of breakthrough points is one with a probability P_1, two with probability P_2 and three with probability P_3 (see Fig. 7b in Ceballos et al. (2011)) with $P_1 + P_2 + P_3 \approx 1$ provided that N_x is not too small. Hence, the probability of having more than three breakthrough points is negligible. Thus, the prefactor N_e should be equal to $N_e \approx P_1 + 2P_2 + 3P_3$. The numeral value 1.24 is consistent with the values of P_1, P_2, and P_3 reported in Fig. 7b in Ceballos et al. (2011).

Naturally, the consideration of elementary cube becomes meaningless when $N_z \geq N_x$, i.e., $N_z/N_x \geq 1$, which is also consistent with the numerical results. The latter indicates that the scaling given by Eq. (6) actually holds up to $N_z/N_x \approx 0.8$.

The numerical study indicates that the power law behavior does not hold for the ultrathin systems corresponding approximately to $N_z \leq 10$. The variation of probability $\frac{N_{\mathrm{BT}}}{N_x^2}$ with the thickness is slower than predicted by Eq. (7) for $N_z \leq 10$. This reflects the fact that the number of breakthrough points can vary much more than between 1 and 3 from one elementary cube to another when $N_z \leq 10$. This is shown in Fig. 8 in Ceballos et al. (2011) which indicates that the number of breakthrough points follows a Gaussian distribution when $N_z < 10$.

Showing that Eq. (7) (with $N_e \approx 1.24$) overestimates the probability $\frac{N_{\mathrm{BT}}}{N_x^2}$ for the ultrathin systems is easy. To this end, consider a system formed by a single layer of pores ($N_z = 1$) for the case $n_i = 1$. Applying Eq. (7) leads to $\frac{N_{\mathrm{BT}}}{N_x^2} \approx 1.24$. Each pore in this layer is connected to 4 neighbor pores located in the same horizontal plane (we recall that a simple cubic network is considered) and to a vertical inlet bond and a vertical outlet bond. The probability for the liquid to go straight from the inlet bond to the outlet bond (where it forms a breakthrough point) is therefore only 1/5. Thus, it is clear that the total of breakthrough points N_{BT} is necessary significantly lower than $1.24N_x^2$, which is the value given by Eq. (6). A more refined analysis of this probability is as follows. Consider an outlet bond. As just discussed, the probability for this outlet bond to be a breakthrough point because of direct invasion from immediate neighbor inlet bond is 1/5. However, water can also reach the pore adjacent to the considered outlet bond from neighboring pores with probability 2/5 (we consider the sequential algorithm assuming that two of the four neighboring pores have been invaded before the considered pore is activated). Then, the probability of invading the outlet bond from a path originating from the two considered neighbor pores is 1/4 (the inlet bond cannot be invaded). This leads to $\frac{N_{\mathrm{BT}}}{N_x^2} \approx \frac{1}{5} + \frac{2}{5} \times \frac{1}{4} \approx 0.3$, which almost exactly corresponds to the numerical results for $N_z = 1$ in Fig. 2a.

3.3 On the Universal Nature of Results from PN Simulations on Random Networks

In order to confirm that the results discussed in previous sections are generic and not specific to cubic networks, a few simulations were performed over unstructured networks. The

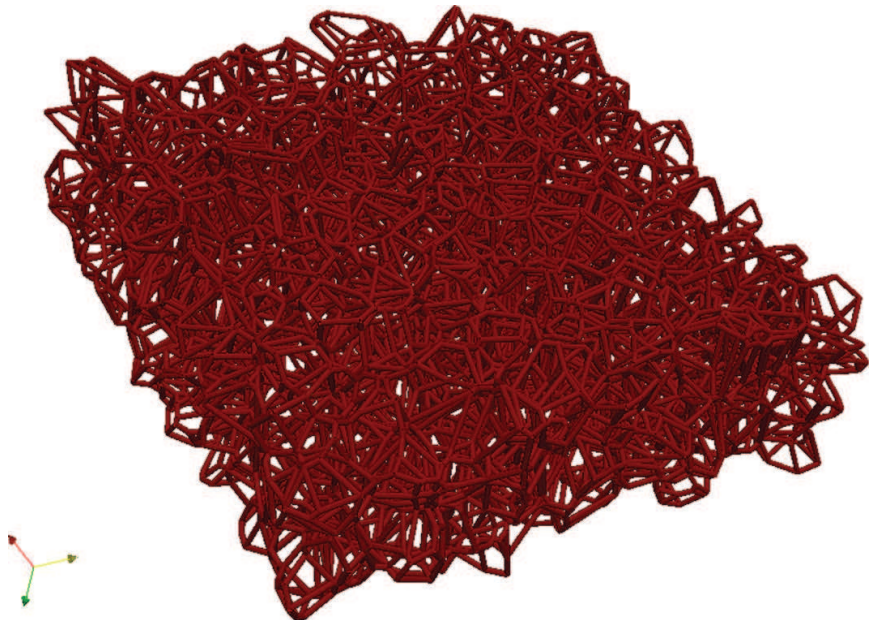

Fig. 6 Example of generated fiber image generated using the method described in Gostick (2013). The *Voronoi lines* (fibers) create polyhedral cages that define pore bodies

model used in this section has a random 3D architecture based on Delaunay tessellations to represent the pore space and Voronoi tessellations to represent the fiber structure. This model is illustrated in Fig. 6 (see also Fig. 5), and the procedure for generating it is described in detail in Gostick (2013). This procedure is therefore not described again here. This type of network is referred to as a Voronoi network in the following.

Similarly as for the cubic network, N_z is the number of pores (a pore corresponds to a polyhedral cage in Fig. 6) in the through plane direction, whereas N_x is the number of cages (pores) in the in-plane directions ($N_y = N_x$).

Figure 7 shows the average number of breakthrough points N_{BT} as a function of porous layer relative thickness N_z/N_x when all pores are active at the inlet ($n_i = 1$) obtained for Voronoi networks of lateral size $N_x = 30$ and $N_x = 40$, respectively.

As can be seen from Fig. 7, the results obtained with the Voronoi network are consistent with the power law behavior obtained with the cubic network. In particular, the data for the network size $N_x = 40$ are consistent with the exponent 2 of the power law. The conclusion is that the results shown in Fig. 7 are a sufficiently clear indication that the results discussed in previous sections are generic of thin systems.

4 Fine Layer

The average pore size in the thin layer is much smaller than in the coarse layer. As an example, consider a thin layer of 50 μm in thickness and of 2.6 mm in lateral size. The lattice spacing a_{f} is 700 nm. The fine layer is thus represented by a $3715 \times 3715 \times 72$ pore network ($N_{x\mathrm{f}} = N_{y\mathrm{f}} = 3715$, $N_{z\mathrm{f}} = 72$). Pore network simulations in such a big network would be computationally extremely long, if even feasible. Therefore, the fact of knowing "universal" laws is here crucial. Note that the subscript "f" is used to label the data relative to the fine layer.

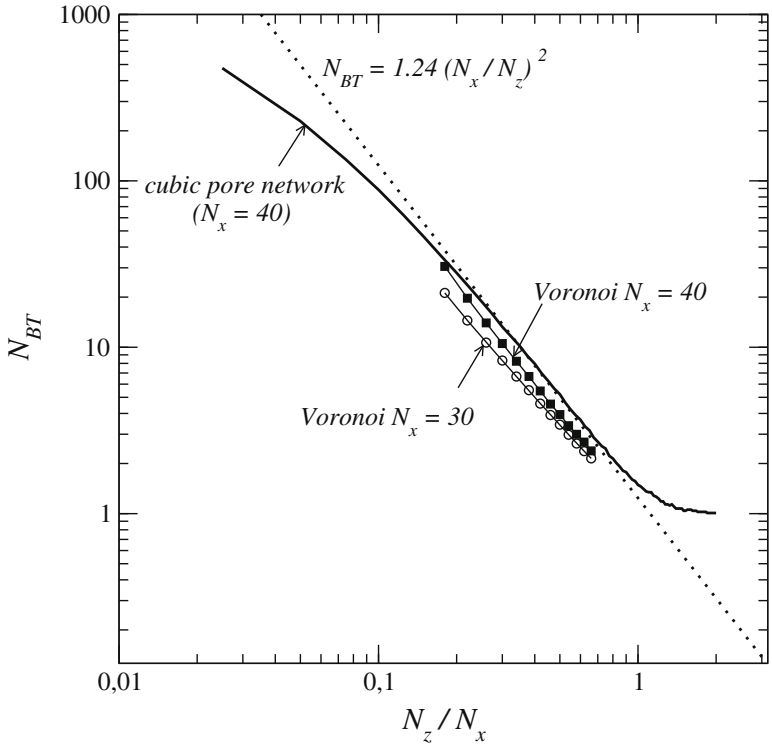

Fig. 7 Average number of breakthrough points N_{BT} as a function of porous layer relative thickness N_z/N_x when all pores are active at the inlet ($N_i = N_{\max}$) ($n_i = 100\,\%$). The results are shown for two Voronoi network lateral sizes ($N_x = N_y = 30$ and $N_x = N_y = 40$, averaged over 1500 realizations) together with the results for a cubic network of lateral size $N_x = N_y = 40$

4.1 Breakthrough Points

In relation with the results shown in Fig. 2, we first note that $N_{z\mathrm{f}}/N_{x\mathrm{f}} \leq 0.8$ ($N_{z\mathrm{f}}/N_{x\mathrm{f}} = 0.019$). Thus, the system is in the universal regime. Second, $N_{z\mathrm{f}} \geq 10$. Thus, we can use the power law relationship to obtain the number of breakthrough point. As an example consider the case $n_{i\mathrm{f}} = 1$. Applying Eq. (7) (with $N_e = 1.24$) yields $N_{\mathrm{BT}} \approx 3300$, to be compared with the number of injection points $N_i = 3715^2$. Hence, $N_{\mathrm{BT}}/N_i \approx 2 \times 10^{-4}$, which illustrates the efficiency of liquid path coalescence process. Also it can be noted that the thickness corresponding to the end of the power law regime, i.e., $N_{z\mathrm{f}}/N_{x\mathrm{f}} \approx 0.8$ corresponds to $N_{z\mathrm{f}} \approx 2972$ for this network lateral size. Similarly, other properties such as the overall saturation and the diffusion coefficient can be predicted using the data obtained from the simulations over much smaller networks presented in Sect. 2. How to construct these data is the main objective of the present section.

4.2 Overall Liquid Saturation

The objective is to determine the variation of S_{f} as a function of $N_{z\mathrm{f}}$ for different fraction $n_{i\mathrm{f}}$ in the range [0.02, 0.9]. Figure 3 shows the results obtained with networks of size $20 \times 20 \times N_z$ and $40 \times 40 \times N_z$. The obvious and expected result is that the saturation increases with increasing n_i for a given thickness. There is absolutely no reason to expect a different tendency in a large network such as the $3715 \times 3715 \times N_{z\mathrm{f}}$ network used to represent the fine layer.

One problem is that the results shown in Fig. 3 cannot be directly applied because the variation of S_{f} with thickness $N_{z\mathrm{f}}$ and $n_{i\mathrm{f}}$ also depends on lateral size $N_{x\mathrm{f}}$ for $N_{z\mathrm{f}} > 20$. The situation is as follows. For $N_{z\mathrm{f}} < 20$, the variation of S_{f} with $N_{z\mathrm{f}}$ is independent of lateral size $N_{x\mathrm{f}}$, and thus, the values determined on network of relatively small lateral extensions and

shown in Fig. 3 are also the ones expected with a large network in this range of thicknesses. For $N_{zf} \approx 2\, N_{xf}$, there is only one breakthrough point and there is a clear dependence of saturation with lateral size N_{xf} as also illustrated in Fig. 3. Since the system is at the percolation threshold (only one breakthrough point) at $N_{zf} \approx 2\, N_{xf}$, it is tempting to make use of the percolation scaling $S \propto N_x^{d_f-3}$, where d_f is the fractal dimension of the percolation cluster ($d_f = 2.52$ in 3D). According to the results presented in Ceballos et al. (2011), see the inset in Fig. 12b in this reference, this is a quite reasonable idea. Thus, suppose we know the saturation S_{Nx1} at $N_{z1} \approx 2\, N_{x1}$ for a network of lateral size N_{x1} then the saturation S_{Nx2} at $N_{z2} \approx 2\, N_{x2}$ for a network of lateral size N_{x2} is expected to be

$$S_{Nx2} \approx S_{Nx1} \left(\frac{N_{x1}}{N_{x2}} \right)^{3-d_f}, \tag{8}$$

which consistently with available numerical simulations predicts that S at $N_{zf} \approx 2\, N_{xf}$ decreases with increasing lateral size (this is illustrated in Fig. 3).

From the data available for networks of lateral size $N_x = 40$, we therefore know for any larger size the saturation for the thicknesses lower than 20 (there are identical to the ones for the network of lateral size 40) and the saturation at $N_{zf} \approx 2\, N_{xf}$, which is given using obvious notations by $S_f(2N_{xf}) = S_f(2N_{x40}) \left(\frac{N_{x40}}{N_{xf}} \right)^{3-d_f}$. For our network of lateral size $N_{xf} = 3715$, this means that we know the saturations for the thickness lower than 20 and at $N_{zf} = 7430$. The question is then how to estimate the saturation between $N_{zf} = 20$ and $N_{zf} = 7430$.

From the shape of the curves shown in Fig. 3, we decided to perform power law adjustments, i.e.,

$$S_f = \eta N_{zf}^{\chi} \tag{9}$$

between the values limiting the range of variations of S_f. This gave the variations shown in Fig. 8, whereas the values of coefficients of the power law adjustments for the various n_{if} are given in Table 1

4.3 Diffusion Coefficient

The next step is to evaluate the effective diffusion coefficient of the fine layer for the various n_{if}. Figure 4 shows the variations obtained from simulations on networks of size $20 \times 20 \times N_z$ and $40 \times 40 \times N_z$. A natural idea based on the approach prevailing for traditional porous media is to try to express D^* as a function of liquid saturation S. However, combining the results of Figs. 3 and 4 leads to the results shown in Fig. 9. Interestingly, contrary to traditional porous media, there is not a one to one relationship between D^* and S. This is another illustration of the scale dependence of results in a thin system for the situation considered in the present article. See also García-Salaberri et al. (2015) for further discussion on the relationship between D^* and S in thin systems.

Since searching for simple relationships between D^* and S is not appropriate here, we proceed similarly as for constructing the saturation profiles. This means that we are interested in the variation of D^* as functions of N_{zf} and n_{if} rather than S.

As illustrated in Fig. 4, we first note that the values of D_f^* are independent of lateral size N_{xf} for $N_{zf} < 20$. Then, we estimate D_f^* for $N_{zf} = 2N_{xf}$. For this thickness, we know that the invading phase, i.e., the liquid phase, forms a percolation cluster (there is only one breakthrough point). The defending phase (the gas phase) is therefore well connected (except of course when n_{if} approaches 100 %). In others terms, the gas phase is far from a percolation threshold and thus traditional relationship expressing the variation of D_f^* with saturation

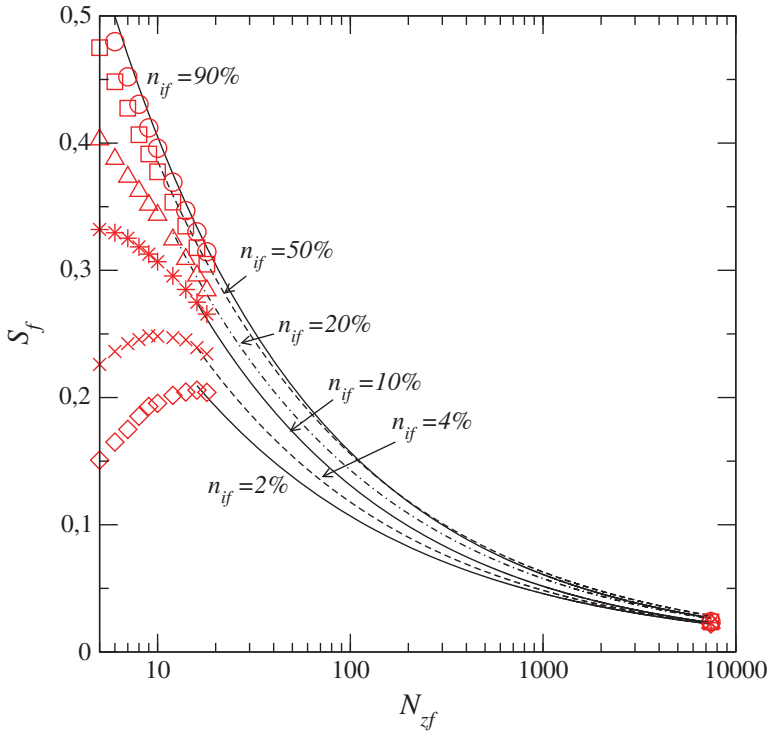

Fig. 8 Constructed variation of overall saturation as a function of layer thickness for various fractions of inlet injection bonds n_{if} for the 3715 × 3715 × N_{zf} network used to represent the fine layer. The *symbols on the left* corresponds to the "universal" values (i.e., independent of lateral size) obtained on a smaller network for $N_{zf} < 20$. The *symbols on the right* corresponds to the saturations computed using the percolation scaling [Eq. (8)]. These saturations are actually very close for the various n_{if} and the *symbols on the right* are therefore almost superposed one on top of another. The *lines* correspond to the power law adjustments [Eq. (9), see text]

Table 1 Coefficients of power law [Eq. (9)] for various n_{if}

n_{if} (%)	η	χ
2	0.579	−0.367
4	0.697	−0.386
10	0.840	−0.403
20	0.877	−0.355
50	0.956	−0.394
90	1.044	−0.411

should be acceptable for this thickness. As an example we took a classical relationship of the form,

$$\frac{D_f^*(S_f)}{D} = \alpha(1 - S_f)^{1.5} \tag{10}$$

and determined the numerical coefficient α from the results of invasion percolation simulations reported in Ceballos and Prat (2013). This gave $\alpha = 0.23$.

Equation (10) is used to determine D_f^* at $N_{zf} = 2N_{xf}$ from the saturations determined for this thickness as explained previously [i.e., using Eq. (8)].

Then from the shape of the curves shown in Fig. 4, we again decided to perform power law adjustments, i.e.,

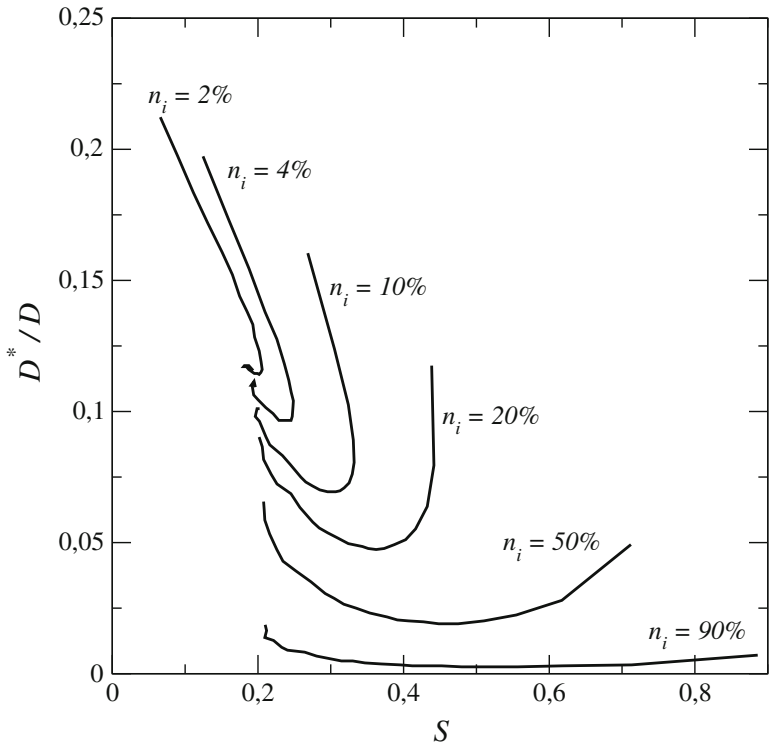

Fig. 9 Variation of diffusion coefficient with saturation for various fractions of inlet injection bonds n_i from simulations on $40 \times 40 \times N_z$ networks. The *curves* are obtained by combining the data shown in Figs. 3 and 4 for the $40 \times 40 \times N_z$ networks

$$\frac{D_{\mathrm{f}}^{*}}{D} = \eta_D N_{z\mathrm{f}}^{\chi_D} \tag{11}$$

between the values limiting the range of variations of D_{f}^{*}. This gave the variations shown in Fig. 10, whereas the values of coefficients of the power law adjustments for the various $n_{i\mathrm{f}}$ are given in Table 2

5 Fine Layer–Coarse Layer Assembly

The objective of this section is to show how the behavior of the fine layer–coarse layer assembly can be predicted from the results presented in the previous sections taking advantage of the established "universal" laws. Also, the objective is to illustrate why the presence of the fine layer can be extremely beneficial to gas access across the coarse layer.

A first problem lies in the nature of the assembly. Here we make the simple assumption that the interface between the fine layer and the coarse layer is sharp. In other terms, this interface has no particular properties. This point is further commented in Sect. 5.

As before, we are interested in the number of breakthrough points at the outlet of coarse layer, the overall saturations in the layers and the gas access through the assembly.

The dimensions and other properties of the fine layer are those given in Sect. 3. As an example, we consider a coarse layer of 200 μm in thickness with a lattice spacing a_{c} of 40 μm. This corresponds to a $65 \times 65 \times 5$ network. Thus, we have a $65 \times 65 \times 5$ network coupled with a $3715 \times 3715 \times N_{z\mathrm{f}}$ network, where $N_{z\mathrm{f}}$ is the thickness of the fine layer (measured in fine layer lattice spacing unit a_{f}).

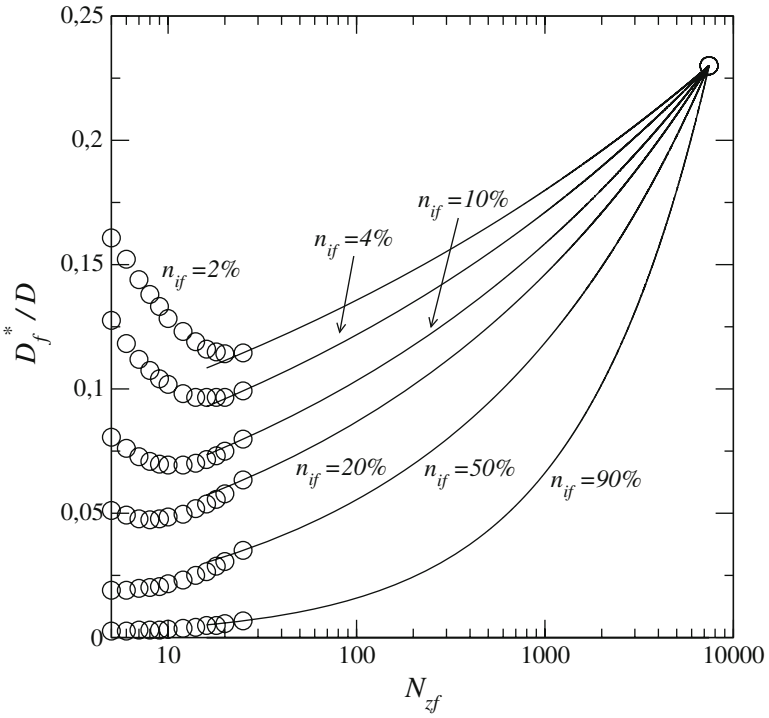

Fig. 10 Constructed variation of diffusion coefficient as a function of layer thickness for various fractions of inlet injection bonds n_{if} for the $3715 \times 3715 \times N_{zf}$ network used to represent the fine layer. The *symbols on the left* corresponds to the "universal" values (i.e., independent of lateral size) obtained on a smaller network for $N_{zf} < 30$. The *symbol on the right* corresponds to the saturations computed using the percolation scaling [Eq. (8)]. These saturations are actually very close for the various n_{if} leading to indiscernible variations at $N_{zf} = 2\,N_{xf}$ (=7430) for the various values of n_{if}. The *lines* correspond to the power law adjustments [Eq. (11), see text]

Table 2 Coefficients of diffusion coefficient power law [Eq. (11)] for various n_{if}

n_{if} (%)	η_D	χ_D
2	0.772	0.122
4	0.617	0.148
10	0.439	0.186
20	0.306	0.226
50	0.121	0.330
90	0.0091	0.620

The reference case is the case where there is no fine layer and all bonds at the coarse layer inlet are injection points ($n_{ic} = 1$). The impact of the fine layer on transport in the coarse layer is illustrated by varying the thickness of the fine layer without modifying the coarse layer.

5.1 Impact of Fine Layer Thickness on the Number of Breakthrough Points at Coarse Layer Outlet

We are first interested in the minimal fine layer thickness N_{zfmin} above which the gas transfer becomes possible across the assembly.

According to Eq. (1), the number of breakthrough points N_{BTf} at the fine layer–coarse layer interface can be expressed as,

$$N_{BTf}/N_{xf}^2 = f(N_{zf}, n_{if}) \quad \text{if} \quad N_{zf} \leq 0.8\,N_{xf} \tag{12}$$

The number of inlet bonds at the inlet of coarse layer is $N_{x\mathrm{c}}^2$. Assuming that the fine layer breakthrough points are evenly distributed at the fine layer–coarse layer interface, we can first estimate the fine layer thickness $N_{z\mathrm{fmin}}$ for which the number of fine layer breakthrough points is about equal to the number of inlet bonds at the coarse layer inlet. This thickness is given by the equation,

$$N_{\mathrm{BTf}} = f(N_{z\mathrm{fmin}}, n_{i\mathrm{f}}) N_{x\mathrm{f}}^2 = N_{x\mathrm{c}}^2 \tag{13}$$

As discussed in Sect. 2, $f(N_{z\mathrm{f}}, n_{i\mathrm{f}}) \approx \frac{1.24}{N_{z\mathrm{f}}^2}$ independently of $n_{i\mathrm{f}}$ as long as $N_{z\mathrm{f}}$ is greater than about 20 (over the range [0.02–1] of n_i considered in Ceballos et al. 2011). Under these circumstances, we deduce from Eq. (13) that,

$$N_{z\mathrm{fmin}} \approx 1.1135 \frac{N_{x\mathrm{f}}}{N_{x\mathrm{c}}} \tag{14}$$

In our case ($N_{x\mathrm{f}} = 3715$, $N_{x\mathrm{c}} = 65$), this gives $N_{z\mathrm{fmin}} \approx 63$. Hence, $N_{z\mathrm{f}}$ must be greater than $N_{z\mathrm{fmin}}$ for having gas percolating paths across the coarse layer–fine layer assembly. For $N_{z\mathrm{f}} \leq N_{z\mathrm{fmin}}$, all inlet bonds at the inlet of coarse layer are invaded by liquid, which blocks the gas access.

The situation $N_{z\mathrm{f}} \leq N_{z\mathrm{fmin}}$ also corresponds to a maximum of breakthrough points at the outlet of coarse layer since all coarse layer inlet bonds are injection bonds.

To determine the number N_{BTc} of breakthrough points at the coarse layer outlet for $N_{z\mathrm{f}} > N_{z\mathrm{fmin}}$, we first have to determine the fraction $n_{i\mathrm{c}}$ of coarse layer inlet bonds which are injection bonds. Again we assume that the fine layer breakthrough points are evenly distributed at the fine layer–coarse layer interface, which leads to,

$$n_{i\mathrm{c}} = \frac{N_{\mathrm{BTf}}}{N_{x\mathrm{c}}^2} = \frac{1.24}{N_{z\mathrm{f}}^2} \frac{N_{x\mathrm{f}}^2}{N_{x\mathrm{c}}^2} \tag{15}$$

Then, we need to know how N_{BTc} varies for fixed coarse layer dimensions ($N_{x\mathrm{c}} = 65$, $N_{z\mathrm{c}} = 5$) as a function of $n_{i\mathrm{c}}$. According to the results reported in Ceballos et al. (2011), the coarse layer is sufficiently thin for the "universal" behaviors characterized in Ceballos et al. (2011) to apply. So we made a fit of the data reported in Ceballos et al. (2011) for the case $N_z = 5$ to obtain,

$$\frac{N_{\mathrm{BTc}}}{N_{x\mathrm{c}}^2} = \frac{2.585 \ln(100 n_{i\mathrm{c}}) + 4.4605}{400} \tag{16}$$

Combining Eqs. (15) and (16) leads to the desired relationship between the number of breakthrough points at the outlet of the assembly as a function of fine layer thickness,

$$\frac{N_{\mathrm{BTc}}}{N_{x\mathrm{c}}^2} = \frac{2.585}{400} \ln\left(\frac{124}{N_{z\mathrm{f}}^2} \frac{N_{x\mathrm{f}}^2}{N_{x\mathrm{c}}^2}\right) + \frac{4.4605}{400} \tag{17}$$

Applied to our example, this leads to the results shown in Fig. 11. As can be seen, increasing $N_{z\mathrm{f}}$ above $N_{z\mathrm{fmin}}$ has a clear impact on the number of breakthrough points at the coarse layer outlet. The number of breakthrough points is decreasing with an increasing fine layer thickness, which is first indication that the presence of a sufficiently thick fine layer should improve the gas access.

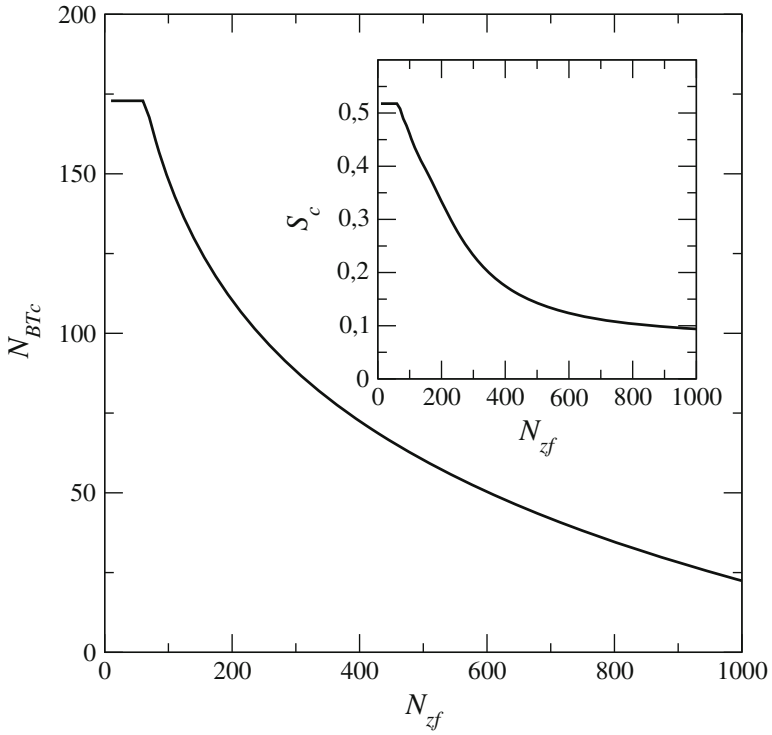

Fig. 11 Number of breakthrough points at the coarse layer outlet as a function of fine layer thickness $N_{z\mathrm{f}}$. As an order of magnitude, 100 breakthrough points correspond to a density of 15 droplets per mm^2 at the surface of the assembly for our example. The inset shows the mean overall liquid saturation in coarse layer as a function of fine porous layer thickness $N_{z\mathrm{f}}$

5.2 Impact of Fine Layer Thickness on Overall Liquid Saturation in Coarse and Fine Layer

For evaluating the evolution of global saturation S_{c} in the coarse layer, we need again a relationship between S_{c} and $n_{i\mathrm{c}}$ for a fixed network size in the "universal" domain. As can be seen from Fig. 3, S_{c} only depends on $n_{i\mathrm{c}}$ for $N_z = 5$ (and thus does not depend on lateral dimension). The variation of S_{c} with $n_{i\mathrm{c}}$ for this thickness is shown in Fig. 12. We then made a polynomial fit from the data reported in Ceballos et al. (2011) and shown in Fig. 12 in order to easily compute S_{c} as a function of $n_{i\mathrm{c}}$.

Combined with Eq. (15), this leads for our example to the results depicted in the inset in Fig. 11 showing the variation of overall saturation in coarse layer as a function of fine layer thickness.

As can be seen, increasing the fine layer thickness significantly decreases the liquid saturation in coarse layer when $N_{z\mathrm{f}} > N_{z\mathrm{fmin}}$. As depicted in Fig. 8, the effect of thickness increase is also to reduce the overall saturation in the fine layer. An interesting difference between the fine and the coarse layer is that the variation of saturation in the coarse layer for a given assembly (i.e., a given fine layer thickness) is independent of $n_{i\mathrm{f}}$ (for the range of $n_{i\mathrm{f}}$ considered), whereas the saturation in the fine layer does depend on $n_{i\mathrm{f}}$ (as illustrated in Fig. 8).

5.3 Impact of Fine Layer Thickness on Gas Access and Gas Transport

As discussed in Sect. 5.1, the fine layer thickness $N_{z\mathrm{f}}$ must be greater than $N_{z\mathrm{fmin}}$ for the gas transfer to be possible across the assembly. Note that the gas transfer as a dissolved species in

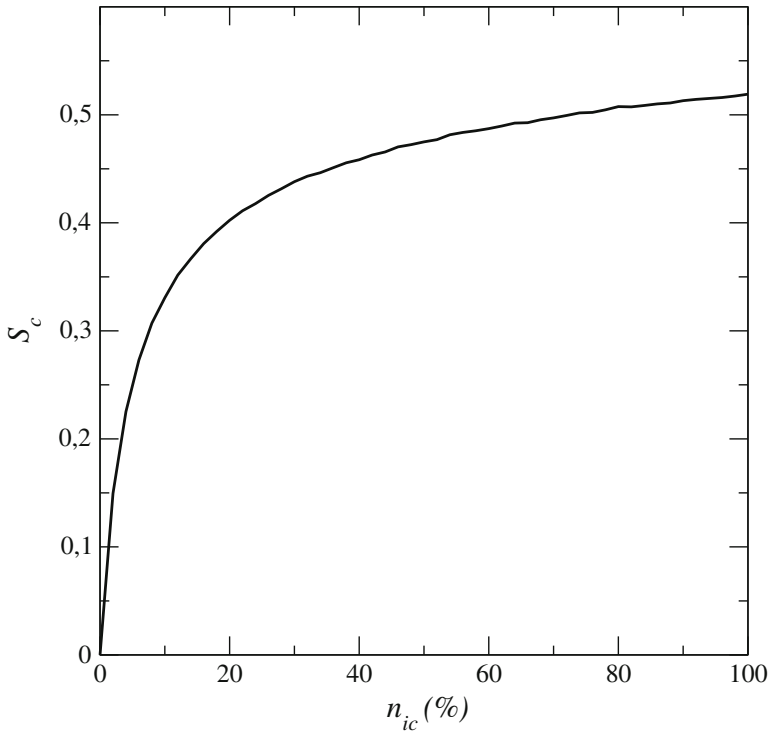

Fig. 12 Mean overall liquid saturation in coarse layer as a function of fraction of injection bonds at layer inlet

the liquid is not considered. Thus, gas transfer is only possible when the gas phase percolates through the assembly. For $N_{zf} \leq N_{zfmin}$, all inlet bonds at the inlet of coarse layer are invaded by liquid, which blocks the gas access.

In what follows, we consider again the case of the diffusive transfer of species B in the gas phase formed by the binary mixture of two species A and B.

Then, the gas access is again characterized by the diffusive flux across the assembly for a given concentration difference Δc imposed across the assembly. This flux, denoted by J, can be expressed as

$$J \approx \left(\frac{H_f}{D_f^*(N_{zf}, n_{if})} + \frac{H_c}{D_c^*(S_c)} \right)^{-1} \Delta c \tag{18}$$

where H_f and H_c are the thicknesses of fine and coarse layers, respectively; $D_f^*(N_{zf}, n_{if})$ and $D_c^*(S_c)$ are the effective diffusion coefficient of fine and coarse layers, respectively. As reference flux, we use the flux across a perfectly dry coarse layer,

$$J_{ref} \approx \frac{D_c^*(0)}{H_c} \Delta c \tag{19}$$

which leads to express Eq. (18) in dimensionless form as

$$\frac{J}{J_{ref}} \approx \left(\frac{H_f}{D_f^*(N_{zf}, n_{if})} + \frac{H_c}{D_c^*(S_c)} \right)^{-1} \frac{H_c}{D_c^*(0)} \tag{20}$$

Equation (20) can be also expressed as

$$\frac{J}{J_{ref}} \approx \left(\frac{N_{zf} a_f}{D_f^*(N_{zf}, n_{if})} + \frac{N_{zc} a_c}{D_c^*(S_c)} \right)^{-1} \frac{N_{zc} a_c}{D_c^*(0)} = \frac{1}{\frac{D_c^*(0)}{D_f^*(N_{zf}, n_{if})} \frac{N_{zf} a_f}{N_{zc} a_c} + \frac{D_c^*(0)}{D_c^*(S_c)}} \tag{21}$$

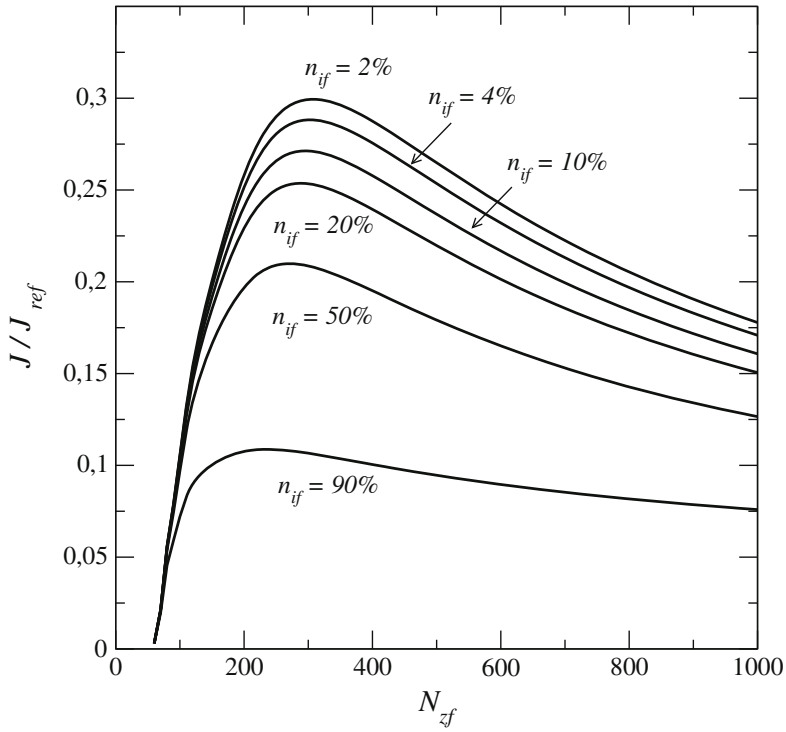

Fig. 13 Variation of gas diffusive flux through the fine layer–coarse layer assembly as a function of fine porous layer thickness $N_{z\mathrm{f}}$ for various fractions of inlet injection bonds $n_{i\mathrm{f}}$

To make use of Eq. (21), we need to know $D_{\mathrm{f}}^{*}(N_{z\mathrm{f}}, n_{i\mathrm{f}})$ and $D_{\mathrm{c}}^{*}(S_{\mathrm{c}})$. For $D_{\mathrm{f}}^{*}(N_{z\mathrm{f}}, n_{i\mathrm{f}})$, we use the results presented in Sect. 4.3 and illustrated in Fig. 10. For the coarse layer, one can directly use the results shown in Fig. 4. From the results shown in Fig. 4 for $N_z = 5$, we can express $D_{\mathrm{c}}^{*}(S_{\mathrm{c}})$ as

$$\frac{D_{\mathrm{c}}^{*}(S_{\mathrm{c}})}{D} = 0.23 - 0.44 S_{\mathrm{c}} \tag{22}$$

Figure 13 shows the variation of J/J_{ref} as a function of $N_{z\mathrm{f}}$ for our example. We first recall that no transfer is possible, i.e., $J = 0.$, in the absence of the fine layer owing to the flooding of coarse layer inlet bonds. Thus, the fine layer has clearly a beneficial effect since it makes possible the gas transfer owing to the impact of fine layer on the number of flooded bonds at the coarse layer inlet. Then, the most striking and interesting result is that the variation of J/J_{ref} is not monotonous but shows a maximum. Thus, there are a range of fine layer thicknesses, around $N_{z\mathrm{f}} = 300$ in Fig. 13, which leads to an optimal gas transfer. Interestingly, the optimal thickness only slightly depends on $n_{i\mathrm{f}}$ over the range of $n_{i\mathrm{f}}$ considered.

To understand the results shown in Fig. 13, one should remember that increasing the fine layer thickness increases the diffusive resistance due to the fine layer but also decreases the diffusive resistance in the coarse layer owing to the decrease in the coarse layer saturation S_{c}. This can further analyzed by expressing Eq. (21) as

$$\frac{J}{J_{\mathrm{ref}}} = \frac{1}{R_{\mathrm{fine}} + R_{\mathrm{coarse}}} \tag{23}$$

where $R_{\mathrm{fine}} = \frac{D_{\mathrm{c}}^{*}(0)}{D_{\mathrm{f}}^{*}(N_{z\mathrm{f}}, n_{i\mathrm{f}})} \frac{N_{z\mathrm{f}} a_{\mathrm{f}}}{N_{z\mathrm{c}} a_{\mathrm{c}}}$ and $R_{\mathrm{coarse}} = \frac{D_{\mathrm{c}}^{*}(0)}{D_{\mathrm{c}}^{*}(S_{\mathrm{c}})}$ represent resistances to diffusive transport in the gas phase in the fine layer and the coarse layer, respectively.

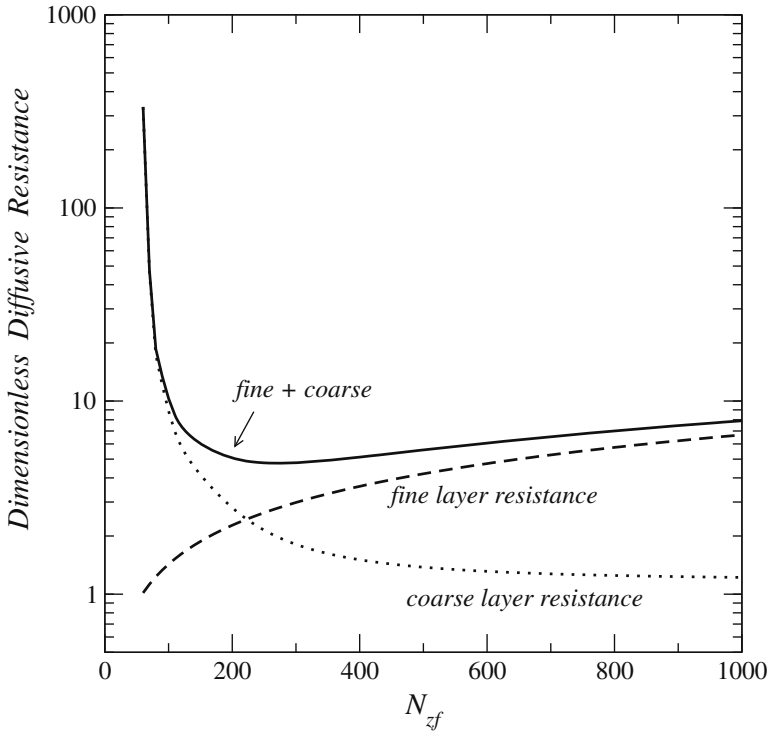

Fig. 14 Variation of fine layer and coarse layer diffusive resistances a function of fine porous layer thickness N_{zf} for the case $n_{if} = 0.5$

As an example, the variations of R_{fine} and R_{coarse} as a function of N_{zf} are shown in Fig. 14 for the case $n_{if} = 0.5$. For sufficiently low N_{zf}, the liquid saturation in the coarse layer is high (see the inset in Fig. 11), close to the saturation corresponding to the gas percolation threshold. As a result, the coarse diffusive resistance is by far dominant. Then, this resistance decreases rapidly with the increase in the fine layer thickness owing to the impact of the fine layer on the coarse layer saturation and diffusion coefficient [see the inset in Fig. 11 and Eq. (22)]. The fine layer resistance progressively increases with N_{zf} until both resistances are comparable. This corresponds to the optimal fine layer thicknesses. Further increase in the fine layer thickness leads to the increase in the overall resistance owing to the increase in fine layer resistance, which progressively becomes the dominant resistance.

6 Discussion

6.1 On the Fine Layer–Coarse Layer Interface

In the present investigation, the interface between the fine layer and the coarse layer was considered as sharp. In fact, we implicitly assumed that the two layers could be prepared independently and then just press one onto the other with negligible deformation and negligible overlap between the two layers. However, in practice, the fine layer is often obtained by depositing and agglomerating fine particles on the coarse layer. As a result a non-negligible fraction of the fine layer can actually penetrate into the coarse layer. Under these circumstances, the system can actually be described in terms of at least three regions: the region of the coarse layer far from the fine layer which is free from fine layer material, the fine layer formed as a result of the agglomeration of particles and a transition region where both solid phase belonging to the coarse layer and the fine layer material are present together.

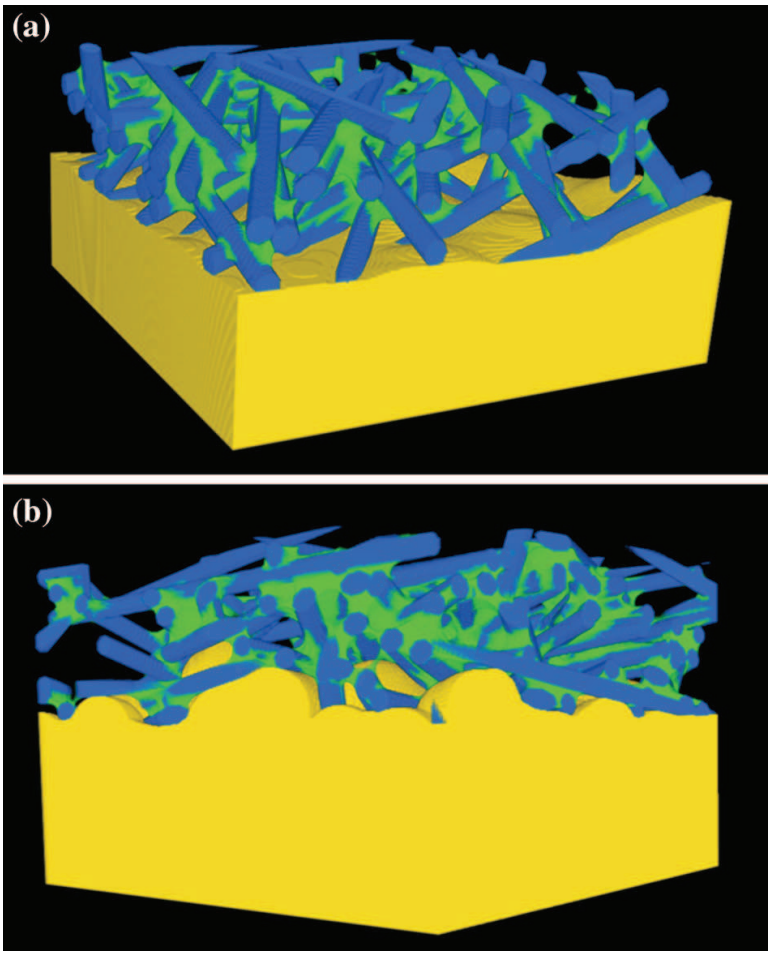

Fig. 15 **a** Illustration of the situation considered in the present article where the transition between the fine layer (in *yellow*) and the coarse layer (represented as a fibrous material with fiber in *blue* and binder in *green*) is sharp, **b** illustration of the situation with interpenetration of the fine layer and the coarse layer

This is illustrated in Fig. 15b. Thus, as discussed in Prat and Agaësse (2015), the interfacial region between the two layers must then be considered as a transition region between the two regions. The transition region was referred to as the "third layer" in Prat and Agaësse (2015). In contrast to the sharp interface, transport properties must be determined also for the transition region. It can be surmised that the transition region can have a great impact on transport properties on the whole assembly. This of course depends notably on the thickness of transition region compared to the thicknesses of the two other regions. It is difficult to go further without considering a specific example. Thus, here the message is simply that the fine layer–coarse layer assembly we have considered in the previous section can be an overly simplified representation of the assembly and that further work is needed to study systems such as the one illustrated in Fig. 15b.

6.2 Comparison with a Previous Work

Interestingly, a problem similar to the one considered in Sect. 5 was studied in Nam and Kaviany (2003) but using traditional volume average equations, such as the generalized Darcy's law. As in the present work, they found a range of fine layer thicknesses optimizing the gas diffusion transport. However, the impact of the fine layer was quite weak. By contrast, the impact is quite significant in our study. To explain the difference, we first note that

considering discrete injection points cannot be made accurately within the framework of the continuum approach. More importantly, the relevance of traditional continuum approach for studying the considered problem is highly questionable. This is discussed in Rebai and Prat (2009). First, there is an obvious lack of length scale separation as regards the coarse layer (only five pore sizes thick in our example). Second, it is well known that the capillarity-dominated regime considered in the present work and which is also supposed to prevail for the case studied by Nam and Kaviany (2003) is a regime that cannot be described properly with the traditional continuum two-phase flow model (e.g., Rebai and Prat 2009; Lenormand et al. 1988). This is an example of thin porous medium specificity; i.e., traditional concepts can be inappropriate or at best can lead to very approximate results.

6.3 Applications to PEMFC

This section can be skipped by readers not familiar with PEMFC. In the context of PEMFC, the coarse layer corresponds to the gas diffusion layer (GDL), the fine layer to the microporous layer (MPL). First, it can be noted that we considered a scenario in which liquid water forms in the catalyst layer (the catalyst layer (CC) is a fine porous layer adjacent to the MPL where the electrochemical reaction takes place and water is produced). Although this scenario has been considered in many papers, it is now widely admitted that liquid–vapor-phase change phenomena, e.g., evaporation and condensation, are also a key factor in this system (e.g., Straubhaar et al. 2015 and references therein). If one accepts that liquid water enters the MPL–GDL assembly from the CC, then the consideration of multiple independent injection points at the inlet comes from the fact that water formed in different points within the volume of the CC (e.g., Ceballos and Prat 2010; El Hannach et al. 2011, 2012 for more details).

Experimental studies have shown that the presence of the MPL had a beneficial impact on the fuel cell performance (e.g., Qi and Kaufman 2002; Chen et al. 2004; Kang et al. 2010). The present study provides a piece of explanation in relation with the general problem of the water management in PEMFC. In brief, adding the MPL improves the oxygen access to the CC and reduces the risk of flooding of the GDL.

However, the situation in a fuel cell is more complex than considered in the present study. For example, the GDL outlet surface is not entirely free. A significant fraction of this surface is occluded by the ribs of the bipolar plate. The GDL is compressed differently below the rib and below the channel. We considered isotropic networks, whereas the GDL is an anisotropic medium. Also, considering a thick transition region (as discussed in Sect. 5.1) would be more realistic. The GDL is often considered as only partially hydrophobic (e.g., Ceballos and Prat 2013), whereas we have assumed a perfectly hydrophobic assembly. Cracks are often present in the MPL contrary to what we assumed. In brief, several aspects need to be incorporated in the modeling for extending the results presented in the present paper. All these might explain why the optimum fine layer was predicted to be 250 μm in our study, which is very thick for fuel cells, which have GDL+MPLs in that range. Nevertheless, we believe that the present work well illustrates one of the possible beneficial impacts of the MPL–GDL assembly, namely its impact on the gas access, compared to the situation where the MPL is not present.

7 Conclusion

Thin porous media represent a special class of porous media for which classical models based on the traditional continuum approach to porous media cannot be adapted owing to the lack of length scale separation over the thickness.

As an illustrative example, we considered a situation where the thin porous medium was formed by the assembly of a fine layer and a coarse layer. We studied a situation, inspired from a situation considered in relation with the water management problem in PEMFC, where liquid water was injected at the assembly inlet and the gas present at the outlet must percolate through the assembly.

It was first shown how laws or relationships governing different variables of interest could be established from pore network simulations over single layers. Then, these relationships were used to study the impact of fine layer thickness on gas diffusion transport properties of the assembly.

It was showed that the consideration of the fine layer had a beneficial impact on gas transport and that there exists a narrow range of fine layer optimal thicknesses. Furthermore, the optimal thicknesses were found to be only slightly sensitive to the fraction of injection bonds at the fine layer inlet.

Although the main result, i.e., the existence of a range of optimal thicknesses, is expected to be quite general, several points deserve further investigations. For example, the coarse layer thickness was not varied. It is likely that the optimal thickness depends on the coarse layer thickness. More importantly, the data for large networks were extrapolated from data on small networks. Extensive pore network simulations on larger networks than the ones considered in previous works are desirable to confirm the validity of the extrapolation methods proposed in the present work.

A perhaps still more interesting issue in the context of thin porous media would be to analyze more properly the impact of the transition region between the fine layer and the coarse layer. Here we simply assume a sharp interface between the two layers. In many thin systems, the consideration of this interface as a transition region of a certain thickness having specific properties seems more appropriate.

Acknowledgements The research leading to these results has received funding from the European Union's Seventh Framework Programme (FP7/2007-2013) for the Fuel Cells and Hydrogen Joint Technology Initiative under Grant Agreement No. 303452, "IMPACT—Improved Lifetime of Automotive Application Fuel Cells with ultra-low Pt-loading."

References

Barbir, F.: PEM Fuel Cells: Theory and Practice. Elsevier Academic Press, Amsterdam (2005)

Bazylak, A., Berejnov, V., Markicevic, B., Sinton, D., Djilali, N.: Numerical and microfluidic pore networks: towards designs for directed water transport in GDLs. Electrochim. Acta **53**(26), 7630–7637 (2008)

Ceballos, L.: Caractérisation des propriétés fluidiques des couches de diffusion des piles à combustible PEMFC par une approche numérique de type réseaux de pores et par une analyse d'images issues de la tomographie X. Ph.D thesis, University of Toulouse, France (2011)

Ceballos, L., Prat, M.: Invasion percolation with multiple inlet injections and the water management problem in proton exchange membrane fuel cells. J. Power Sources **195**, 825–828 (2010)

Ceballos, L., Prat, M.: Slow invasion of a fluid from multiple inlet sources in a thin porous layer: influence of trapping and wettability. Phys. Rev. E **87**, 043005 (2013)

Ceballos, L., Prat, M., Duru, P.: Slow invasion of a nonwetting fluid from multiple inlet sources in a thin porous layer. Phys. Rev. E **84**, 056311 (2011)

Chen, J., Matsuura, T., Hori, M.: Novel gas diffusion layer with water management function for PEMFC. J. Power Sources **131**, 155–161 (2004)

El Hannach, M., Prat, M., Pauchet, J.: Pore network modelling: application to multiphase transport inside the cathode catalyst layer of proton exchange membrane fuel cell. Electrochim. Acta **56**, 10796–10808 (2011)

El Hannach, M., Prat, M., Pauchet, J.: Pore network model of the cathode catalyst layer of proton exchange membrane fuel cells: analysis of water management and electrical performance. Int. J. Hydrogen Energy **37**(24), 18996–19006 (2012)

Fazeli, M., Hinebaugh, J., Bazylak, A.: Investigating inlet condition effects on PEMFC GDL liquid water transport through pore network modeling. J. Electrochem. Soc. **162**(7), F661–F668 (2015)

García-Salaberri, P.A., Hwang, G., Vera, M., Weber, A.Z., Gostick, J.T.: Effective diffusivity in partially-saturated carbon-fiber gas diffusion layers: effect of through-plane saturation distribution. Int. J. Heat Mass Transf. **86**, 319–333 (2015)

Gostick, J.T.: Random pore network modeling of fibrous PEMFC gas diffusion media using Voronoi and Delaunay tessellations. J. Electrochem. Soc. **160**(8), F731–F743 (2013)

Gostick, J.T., Ioannidis, M.A., Fowler, M.W., Pritzker, M.D.: Pore network modeling of fibrous gas diffusion layers for polymer electrolyte membrane fuel cells. J. Power Sources **173**, 277–290 (2007)

Hinebaugh, J., Fishman, Z., Bazylak, A.: Unstructured pore network modeling with heterogeneous PEMFC GDL porosity distributions. J. Electrochem. Soc. **157**, B1651–B1657 (2010)

Kang, J.H., Lee, K.J., Yu, S.H., Nam, J.H., Kim, C.J.: Demonstration of water management role of microporous layer by similarity model experiments. Int. J. Hydrogen Energy **35**, 4264–4269 (2010)

Lee, K.J., Nam, J.H., Kim, C.J.: Pore-network analysis of two-phase water transport in gas diffusion layers of polymer electrolyte membrane fuel cells. Electrochim. Acta **54**, 1166–1176 (2009)

Lee, K.J., Kang, J.H., Nam, J.H., Kim, C.J.: Steady liquid water saturation distribution in hydrophobic gas-diffusion layers with engineered pore paths: An invasion-percolation pore-network analysis. J. Power Sources **195**(11), 3508–3512 (2010)

Lee, K.J., Kang, J.H., Nam, J.H.: Liquid water distribution in hydrophobic gas-diffusion layers with interconnect rib geometry: an invasion-percolation pore-network analysis. Int. J. Hydrogen Energy **39**, 6646–6656 (2014)

Lenormand, R., Touboul, E., Zarcone, C.: Numerical models and experiments on immiscible displacements in porous media. J. Fluid Mech. **189**, 165–187 (1988)

Markicevic, B., Bazylak, A., Djilali, N.: Determination of transport parameters for multiphase flow in porous gas diffusion electrodes using a capillary network model. J. Power Sources **171**, 706–717 (2007)

Nam, J.H., Kaviany, M.: Effective diffusivity and water saturation distribution in single-and two-layer PEMFC diffusion medium. Int. J. Heat Mass Transf. **46**, 4595–4611 (2003)

Prat, M., Agaësse, T.: Thin porous media. In: Vafai, K. (ed.) Handbook of Porous Media (Chapter 4), 3rd edn. Taylor & Francis, London (2015)

Qi, Z., Kaufman, A.: Improvement of water management by a microporous sublayer for PEM fuel cells. J. Power Sources **109**, 38–46 (2002)

Qin, C.Z., Hassanizadeh, S.M.: Multiphase flow through multilayers of thin porous media: general balance equations and constitutive relationships for a solid–gas–liquid three-phase system. Int. J. Heat Mass Transf. **70**, 693–708 (2014)

Quin, C.: Water transport in the gas diffusion layer of a polymer electrolyte fuel cell: dynamic pore-network modeling. J. Electrochem. Soc. **162**(9), F1036–F1046 (2015)

Rebai, M., Prat, M.: Scale effect and two-phase flow in a thin hydrophobic porous layer. Application to water transport in gas diffusion layers of PEM fuel cells. J. Power Sources **192**, 534–543 (2009)

Sheppard, A.P., Knackstedt, M.A., Pinczewski, W.V., Sahimi, M.: Invasion percolation: new algorithms and universality classes. J. Phys. A Math. Gen. **32**(49), L521–L529 (1999)

Sinha, P.K., Wang, C.Y.: Pore-network modeling of liquid water transport in gas diffusion layer of polymer electrolyte fuel cell. Electrochim. Acta **52**, 7936–7945 (2007)

Straubhaar, B., Pauchet, J., Prat, M.: Water transport in gas diffusion layer of a polymer electrolyte fuel cell in the presence of a temperature gradient. Phase change effect. Int. J. of Hydrogen Energy **40**(35), 11668–11675 (2015)

Wilkinson, D., Willemsen, J.F.: Invasion percolation: a new form of percolation theory. J. Phys. A Math. Gen. **16**, 3365–3376 (1983)

Wu, R., Zhu, X., Liao, Q., Chen, R., Cui, G.-M.: Liquid and oxygen transport in defective bilayer gas diffusion material of proton exchange membrane fuel cell. Int. J. Hydrogen Energy **38**(10), 4067–4078 (2013)